scientific reports

Check for updates

OPEN

Differential gene expression in trabecular bone osteocytes is related to the local strain and strain gradient

Meghana Machireddy[1], Sarah Nano[1], Lucas Debiase[2], Jonathan Lewis[2], Sara Cole[3], Jun Li[4] & Glen L. Niebur[1,2]✉

Osteocytes regulate the response of osteoclasts and osteoblasts to mechanical loading through signaling molecules, the levels of which are controlled by post-translational modification or degradation and by differential gene transcription and translation. The magnitude and mode of bone tissue deformation that elicits a transcriptional response in individual osteocytes in situ has been difficult to quantify. We measured SOST, Wnt11, TNF, and FRZB gene expression in osteocytes within loaded and unloaded control porcine trabecular bone explants using RNAScope® and compared the local tissue level strain and strain gradient—which we used as an indicator of potential poroelastic fluid flow—in the tissue surrounding osteocytes with high vs. low gene expression. The measured expression of all four genes differed between loaded and unloaded explants, on average, with the mean SOST expression level decreasing by 45%. In the loaded explants, gene expression was altered from baseline in about 30% of the osteocytes, and they were surrounded by tissue with higher strain and strain gradient than the 20 to 25% of osteocytes that remained near baseline expression. Both deviatoric strain and hydrostatic strain gradient were sensitive and specific predictors of the mechanobiological response for individual genes as well as combinations. SOST expression was highly related to elevated strain gradient, providing evidence that osteocytes respond to fluid flow in the lacunar-canalicular system.

The study of bone mechanobiology dates to the nineteenth century when Julius Wolff and Wilhelm Roux postulated the functional adaptation of both the size and microstructure of bone in response to applied loads[1–3]. Mechanical loading is essential to normal skeletal development and growth[4–8]. In addition, mechanobiological signaling triggers the repair of damaged bone tissue[9,10], plays a critical role in fracture healing[11–13] and orthopaedic implant fixation[14,15], and has recently been implicated in modulating cancer metastasis to bone[16–18]. Understanding the modes and magnitudes of loads that initiate or maintain cellular response in bone could provide important insight to harness or control this mechanobiological response.

Mechanobiological effects in bone are primarily governed by osteocytes[19–21], although cells in the marrow also respond to loading and can affect bone formation[22–24]. The immediate response of osteocytes to in situ mechanical loading involves calcium signaling[25], along with post-translational modification[26], trafficking, and degradation of proteins[27] involved in osteoblast and osteoclast differentiation and recruitment. A transcriptomic response involving thousands of genes can be measured within hours of mechanical loading, and the number of differentially regulated genes (DRGs) increases for at least 6 h[28] following a single bout of loading and further increases following multiple days of loading[29,30].

An ongoing challenge in osteocyte mechanobiology has been reconciling the response of osteocytes cultured on glass or tissue culture plastic with their in situ behavior. While 30,000 to 50,000 µstrain deformations of the cell membrane are required to affect gene expression and small molecule signaling in osteocyte-like cells on plastic, the strain in bone is normally less than 2000 µ-strain[31,32]. Indeed, trabecular bone tissue undergoes damage when subjected to compressive strains greater than 10,000 µstrain[33–35]. The discrepancy is partially explained by differences in cell shape[36] and substrate stiffness[37,38], which alter osteocyte mechanosensitivty. However, the most plausible explanation is that the strain on the osteocyte processes within the canaliculi is

[1]University of Notre Dame, Bioengineering Graduate Program, Notre Dame, IN, USA. [2]Department of Aerospace and Mechanical Engineering, Notre Dame, IN, USA. [3]Notre Dame Integrated Imaging Facility, Notre Dame, IN, USA. [4]Department of Applied and Computational Mathematics and Statistics, University of Notre Dame, Notre Dame, IN, USA. ✉email: gniebur@nd.edu

highly amplified, either by the heterogeneity of the deformation[39] or by the effects of fluid flow within the annular space between the processes and the canaliculi[40–43]. While the strain associated with altered gene expression and small molecule signaling in osteocytes in fluid flow chambers has been measured, strain levels in bone tissue surrounding osteocytes exhibiting a mechanobiological response have only been estimated from mouse tibial loading experiments[44]. Trabecular bone provides a unique environment to assess the strain magnitudes and modes associated with the osteocyte response, because the complex morphology results in heterogeneous strain and bone formation. In in vivo controlled loading experiments, regions of high and low strain energy density (SED) were more likely to contain forming and resorbing tissue, respectively[45]. However, the probability of bone formation was less than 50%, even at the highest levels of SED, and, similarly, the probability of resorption was less than 50%, even in unloaded regions[45,46]. Conversely, both formation and resorption were present at the extremes of low and high SED, respectively. This untargeted (re)modeling may result from diffusion of signaling molecules away from the source osteocytes, or from mechanobiological signaling in the marrow[22–24,47]. As such, the transcriptomic or proteomic response of individual osteocytes may provide a more precise indicator of the mechanobiological response.

The goal of this study was to quantify the relationship between the expression of mechanically regulated genes in osteocytes withy local tissue strain in situ and to determine both the modes and the magnitudes of strain that drive altered gene expression. Specifically, we subjected porcine trabecular bone explants to controlled mechanical loading, and (1) measured the expression of four genes that are differentially regulated by loading of trabecular bone—SOST, Wnt11, FRZB, and TNF[29]—within individual osteocytes, (2) compared the bone tissue strain and strain gradient surrounding osteocytes with high vs. low expression of each gene, and (3) used receiver operator characteristic curves to identify tissue strain signals and magnitudes that are associated with differential gene expression due to mechanical loading.

Results

We subjected trabecular bone explants to controlled mechanical loading in a custom bioreactor and measured expression of SOST, Wnt11, FRZB, and TNF in individual osteocytes using RNAScope® (ACDBio) (Fig. 1). These genes were chosen because they exhibited more than two-fold differential expression in this bioreactor culture model in a previous study (Supplemental Figs. 2, 3)[29]. RNAScope® probes bind to RNA transcripts, and the number of fluorescent probes is proportional to the number of transcripts. We found that the average fluorescence intensity of the probe channel within the nucleus increases with the number of bound probes (Supplemental Fig. 1), and hence we were able to analyze large numbers of osteocytes by using the intensity within the osteocyte as a measure of gene expression. The mean intensity of Wnt11 probes was 30% higher in loaded explants than in unloaded controls while the intensities of SOST, FRZB, and TNF were 30 to 45% lower in the loaded explants (Supplemental Table 1).

The gene expression in the osteocyte population was heterogeneous in both loaded and unloaded groups (Fig. 2). The histograms of TNF and FRZB intensity in loaded and unloaded samples had similar variance, while the intensity distribution for SOST had a higher variance in the unloaded explants than in the loaded group, with most osteocytes showing lower expression than the unloaded group (Fig. 2b). In contrast, the Wnt11 intensity distribution became bimodal in the loaded group (Fig. 2d). These changes in cell level gene expression mirror

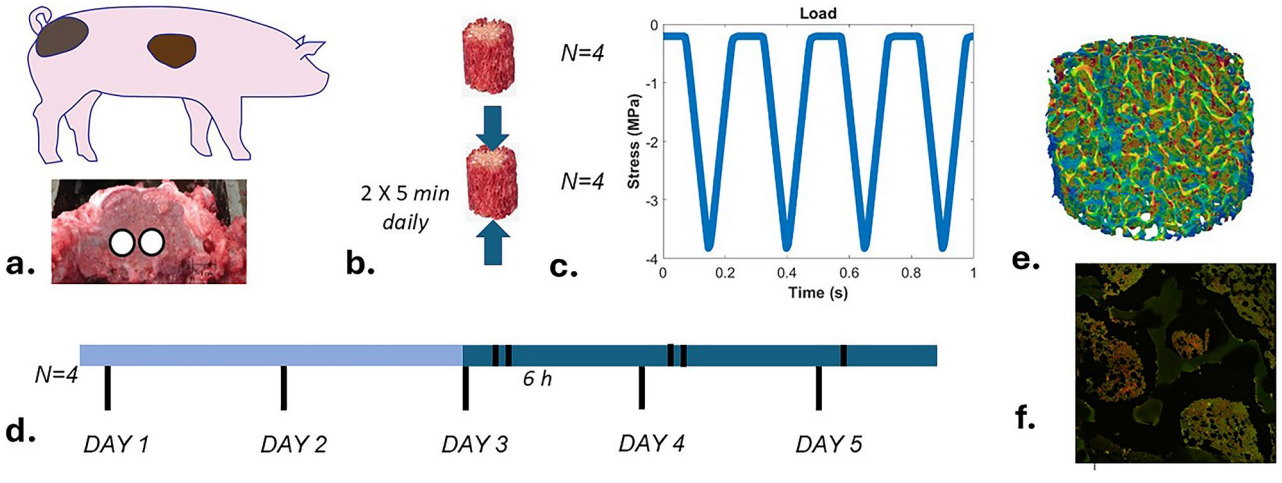

Fig. 1. (**a**) Trabecular bone explants were prepared from the cervical vertebra of young female pigs. (**b**) Samples were cultured in a bioreactor and either subjected to cyclic compression (N = 4) or served as non-loaded cultured controls (N = 4). (**c**) Loaded explants were subjected to 1200 cycles of a rest inserted triangle wave of compressive loading from 10 N to 195 ± 3 N at 4 Hz[48]. (**d**) Explants were loaded twice daily on day 3 and day 4 with a one-hour rest period in between and one time on day 5 and fixed in formalin 6 h after the final loading bout. (**e**) Specimen specific finite element models were created from micro-Computed Tomography scans. (**f**) Fixed explants were processed for histology and in situ hybridization with RNAScope.

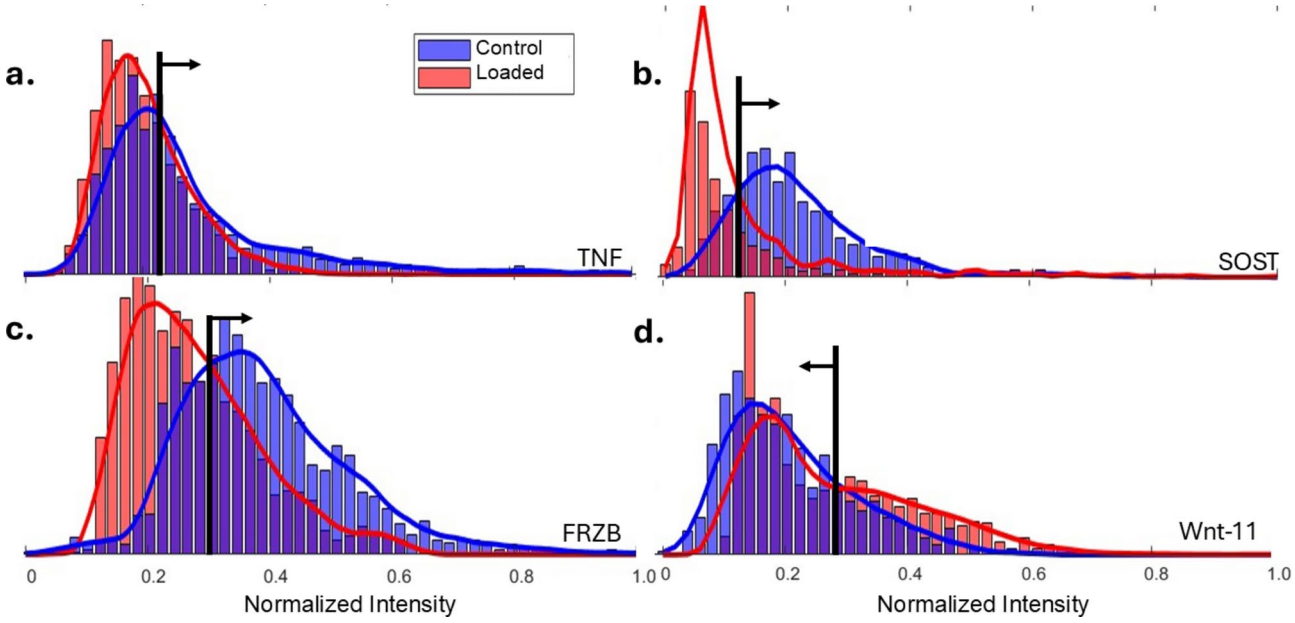

Fig. 2. Probability density functions (PDFs) were fit to the histogram of the mean intensities of isolated osteocytes. The mean intensity of TNF (**a**), SOST (**b**), and FRZB (**c**) probes was higher in the osteocytes in the unloaded samples than in loaded samples while the mean intensity of the Wnt11 probe was higher in the loaded explants (**d**). The intersections of the PDFs of the loaded and unloaded explants were used as thresholds to differentiate between osteocytes that exhibited high vs. low expression of each gene. The arrows indicate the region defined as baseline expression (See data in supplement Table 1).

the changes measured by bulk RNA sequencing (Supplemental Fig. 2)[29], which were further validated by PCR (Supplemental Fig. 3).

We classified osteocytes as having high or low expression of each gene by fitting the histograms using kernel density estimation and finding the intersection between the curves for the loaded and the unloaded groups. In the loaded samples, 50% of the osteocytes had high TNF expression compared to 51% in the controls. In contrast only 43% of osteocytes had high FRZB expression in the loaded group compared to 62% in controls. The proportion of Wnt11-high osteocytes increased to 49% in loaded samples compared to 38% in controls, while the proportion of SOST-high osteocytes decreased to 38% from 72% in loaded vs. control explants.

Specimen specific finite element models were created from micro-computed tomography scans of each loaded explant. We used a mineralization-based modulus assignment and applied the measured displacements from the experiment as a single quasi-static load. The resultant force at the boundary of the explant was not significantly different from the average applied load of 195 ± 3 N (mean ± S.D.), which increases the confidence in our results (Fig. 3).

We registered the confocal images onto cross-sectional images of the finite element results to identify the pixel containing each osteocyte (Fig. 4). Osteocyte lacunae are approximately 10 μm[49], and we mapped each lacuna to a single pixel. We calculated the mean strain and strain gradient in the eight nearest-neighbor pixels at 10 μm resolution. TNF, FRZB and SOST probe intensity were weakly negatively correlated with both deviatoric strain and hydrostatic strain gradient (Spearman's ranked correlation; $p < 10^{-4}$, Table 1). In contrast, Wnt11 expression was weakly positively correlated with deviatoric strain and hydrostatic strain gradient ($p < 10^{-5}$, Table 1). Because most of the tissue was in compression, the hydrostatic strain was negative in most of the tissue and decreased with loading. As such, the correlations were opposite but remained significant (Supplemental Fig. 4).

We compared the mean strain and strain gradient surrounding osteocytes with high vs low expression of each gene. The mean magnitude of the deviatoric and hydrostatic strain were higher by about 24 and 35%, respectively, surrounding osteocytes with high Wnt11 expression ($p < 0.001$, Fig. 5 and Supplemental Table 2). Similarly, deviatoric and hydrostatic strains surrounding TNF-low and FRZB-low osteocytes were higher in magnitude than osteocytes with high (i.e. baseline) expression of each gene ($p < 0.001$; Fig. 5). The deviatoric strain was similarly 24% higher near SOST-low osteocytes, but the hydrostatic strains did not differ ($p > 0.05$). As with the strains, the average strain gradient was higher surrounding Wnt11-high (28%), FRZB-low (34% higher), SOST-low (42% higher) and TNF-low (38% higher) osteocytes. In nearly all cases, the strains and strain gradient had high variances. However, while the strain gradient had a large variance near SOST-low osteocytes, the strain gradient was much lower among SOST-high osteocytes. We further investigated the simultaneous response of pairs of genes to loading using the multiplex kit, which accounted for approximately 30% of the osteocytes (Fig. 5g and k), while 20 to 25% of the cells remained at baseline. The mean mechanical stimuli surrounding cells with two responding genes was higher than that for a single gene, while the stimuli near osteocytes with no responding genes was lower (Supplemental Fig. 5).

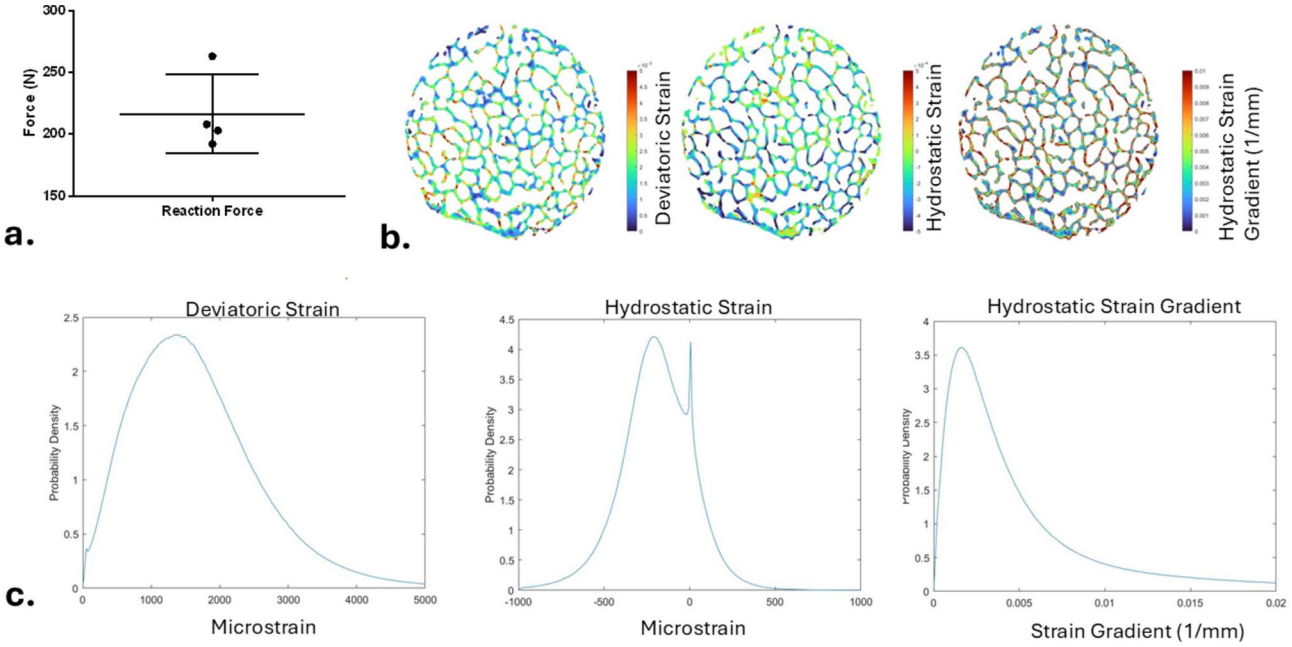

Fig. 3. Finite element models of each loaded explant were created from the micro-CT scans using mineralization based moduli to quantify the strain in the bone tissue. (**a**) The calculated reaction force was 216 ± 42 N which was not significantly different from the applied load of 195 ± 3 N measured during loading. (**b**) Deviatoric strain, hydrostatic strain, and hydrostatic strain gradient were calculated. (**c**) The distribution of each deformation measure.

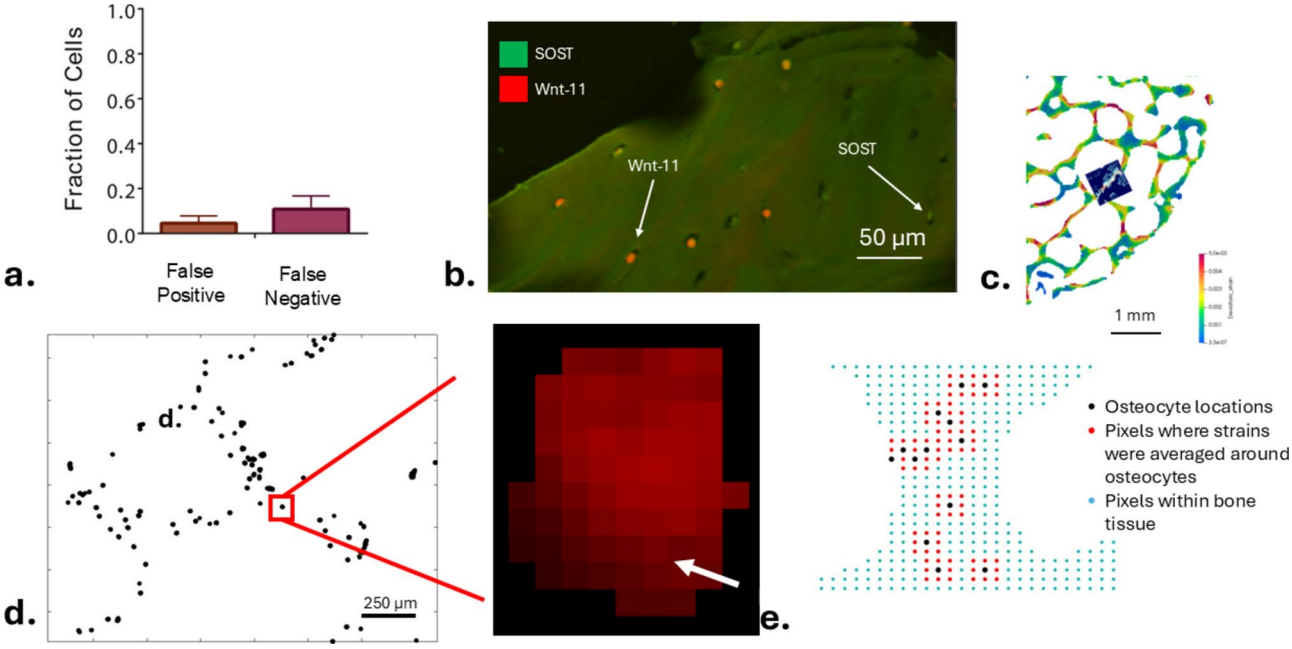

Fig. 4. A custom workflow in ImageJ was used to automatically identify cells in the images. (**a**) 90% of lacunae were accurately identified with a 5% false positive rate. (**b**) An example of a histological section stained for SOST (green) and Wnt11 (red) gene expression. (**c**) The processed images were registered to a single slice of the finite element model and the 10 µm voxel containing each osteocyte was identified. (**d**) Pixels within each cell were identified, and the average brightness of each RNAScope® probe channel was calculated. (**e**) The mean of each strain measure in the eight pixels immediately surrounding each osteocyte was calculated.

	TNF	FRZB	Deviatoric strain	Hydrostatic strain	Hydrostatic strain gradient
TNF	1	0.3509	−0.412	0.333	−0.37
FRZB		1	−0.413	0.303	−0.328
Deviatoric strain			1	−0.725	0.827
Hydrostatic strain				1	−0.5
Hydrostatic strain gradient					1

	SOST	Wnt11	Deviatoric strain	Hydrostatic strain	Hydrostatic strain gradient
SOST	1	−0.149	−0.535	0.364	−0.144
Wnt11		1	0.55	−0.534	0.216
Deviatoric strain			1	−0.859	0.503
Hydrostatic strain				1	−0.623
Hydrostatic strain gradient					1

Table 1. Spearman's ranked correlation coefficients for gene expression and strain measures. All correlations are significant ($p < 10^{-4}$). See Supplemental Fig. 4.

We performed logistic regression between the stimuli and gene expression level (Table 2 and Supplemental Fig. 6). Both hydrostatic strain gradient and deviatoric strain were significant predictors of differential gene expression, but the correlations were weak, with $R^2 < 0.15$ in all cases. Logistic regression for combinations of altered gene expression were similarly significant but weak.

Finally, we plotted Receiver-Operator Characteristic (ROC) curves for gene expression and deviatoric strain and hydrostatic strain gradients and calculated the area under the curve (AUC) as a measure of predictive power (Fig. 6). We found that the AUC was below 0.7 for both deviatoric strain and hydrostatic strain gradient for FRZB, TNF, and Wnt11 expression levels, and were hence relatively weak predictors of gene expression. For SOST, the AUC was 0.723 for hydrostatic strain gradient, and 0.671 for deviatoric strain. When we created ROC curves for osteocytes that either remained at baseline expression or exhibited simultaneous differential expression for both genes in the pair from each multiplex assay (Wnt11 and SOST or FRZB and TNF), the AUC for differential expression of SOST and Wnt11 was 0.788 for deviatoric strain and 0.811 for hydrostatic strain gradient (Fig. 6). For simultaneous differential expression of FRZB and TNF, the AUC was 0.691 for hydrostatic strain gradient and 0.724 for deviatoric strain.

Discussion

We investigated the heterogeneity of the transcriptional response of osteocytes during mechanical loading with respect to several strain measures. We found subsets of osteocytes exhibiting differential SOST, TNF, FRZB, and Wnt11 expression levels between loaded and unloaded bone, as was previously reported for these experimental conditions[29]. There were significant but weak correlations between gene expression and the local strain. However, when we classified the osteocytes as either high or low expression for each gene, the mean deviatoric strain and strain gradient were higher surrounding those with high Wnt11 expression and low FRZB, TNF, or SOST expression than their counterparts, indicating that differential gene expression occurs in those osteocytes located in more highly strained tissue. When we further investigated the subsets of osteocytes where two genes were expressed at levels associated with loading, we found that the surrounding tissue strain was higher than for a single gene response, and much higher than if neither gene responded, suggesting that measuring expression of a single gene within a single cell may not be a reliable measure of osteocyte response. Finally, logistic regressions showed that individual strain measures were a significant but weak predictor of gene expression, and these results were further supported by ROC curves. Notably, SOST gene expression was particularly sensitive to loading, and the hydrostatic strain gradient was the best discriminant of high vs. low SOST expressing cells.

Our study is unique in that we related the response of individual osteocytes to local strain in the surrounding tissue. This allowed us to capture strain and location dependence of gene expression that cannot be detected by bulk sequencing. The in situ model also allowed us to isolate the effects of loading the osteocytes in their native environment while also removing the effect of muscle and soft tissue inflammation, which could result in crosstalk that affects osteocyte gene expression. Moreover, the 3-D model of trabecular bone with controlled loading allowed us to indirectly measure the strain in the tissue surrounding individual osteocytes. By studying trabecular bone where the strain field is heterogeneous, we were able to study osteocytes within a wide range of mechanical environments, although a more porous bone or off-axis loading protocol could have provided even greater variability which would have strengthened our outcomes. We were able to show that the mean intensity of the RNAScope® fluorescent probes within the cell boundary were correlated to the number of probes at high magnification. The resulting fluorescence intensity histograms in the unloaded and loaded samples indicated differential regulation of the four genes following loading as has been previously reported[29]. Finally, our mineralization-based tissue moduli resulted in excellent agreement between the measured mechanical loads and the computational models, suggesting that the strain fields were similarly well captured.

There are also some important limitations to our study. While we were specifically interested in assessing fluid flow in the tissue, we used the surrogate measure of strain gradient. Although computationally tractable, poroelastic models would require the local permeability and boundary conditions at the trabecular surfaces to be assigned. Estimates and even some measurements of these have been published[50], we felt that the associated

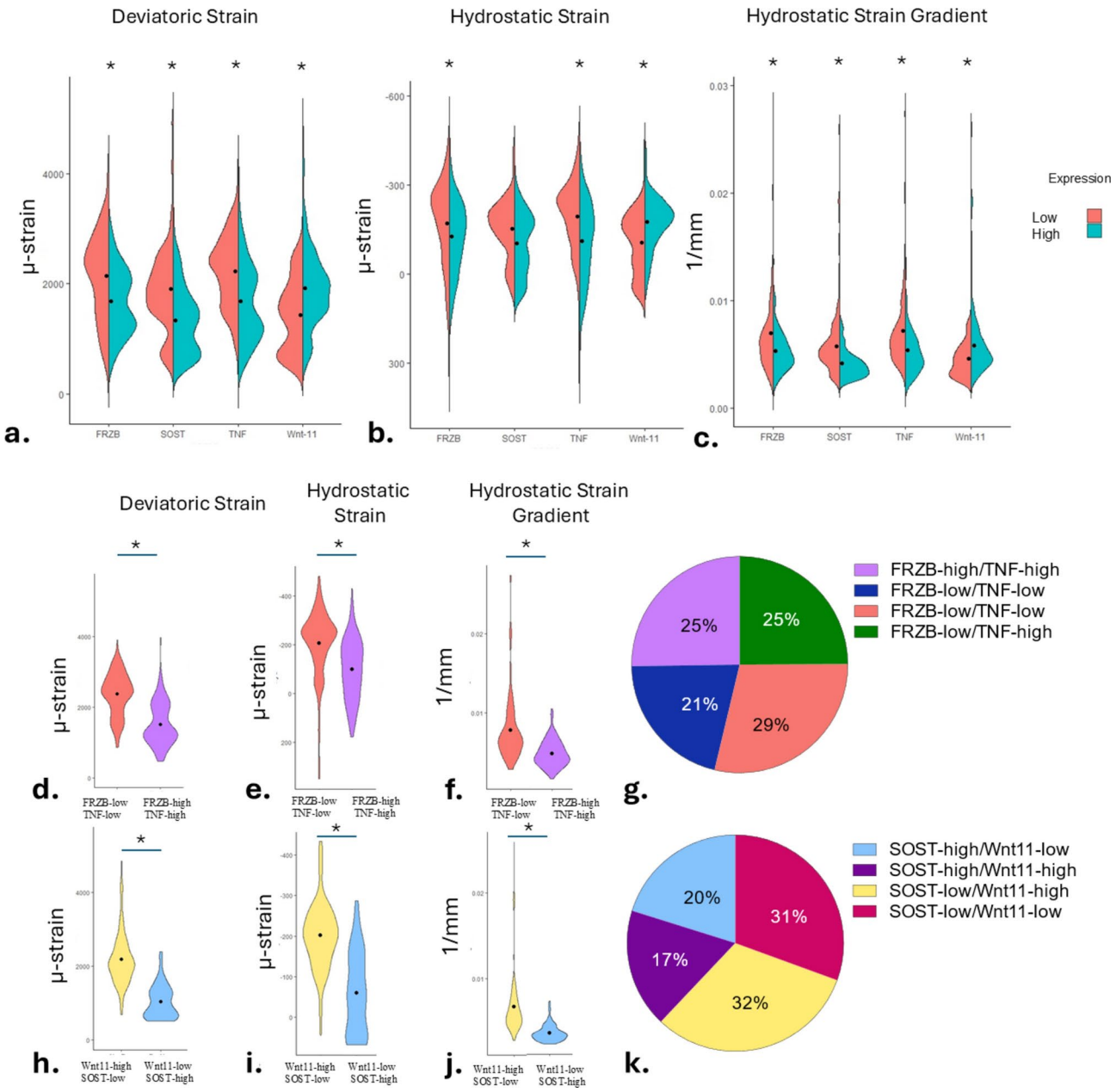

Fig. 5. (**a**) The mean deviatoric strain surrounding FRZB-Low, SOST-Low, TNF-Low, and Wnt11-High osteocytes was higher than that surrounding FRZB-High, SOST-High, TNF-High, and Wnt11-Low osteocytes, respectively (*$p < 0.05$). (**b**) The hydrostatic strain surrounding SOST-High and SOST-Low osteocytes did not differ ($p > 0.05$), while hydrostatic strain gradient (c) was higher surrounding cells with differential gene expression from baseline. Deviatoric strain (**d**) Hydrostatic strain (**e**), and Hydrostatic strain gradient (**f**), were higher near cells with low expression of both FRZB and TNF than near osteocytes that are FRZB-High and TNF-High ($p < 0.5$) corresponding to 29% of osteocytes (**g**). Deviatoric strain (**h**), Hydrostatic strain (**i**), and Hydrostatic strain gradient (**j**) were higher surrounding osteocytes with low SOST and high Wnt11 expression than near osteocytes that were SOST High and Wnt11 Low. (**k**) 32% of osteocytes responded to loading. Note that the hydrostatic strain axes are inverted.

uncertainty did not warrant the added complexity. Similarly, we did not consider viscoelasticity in our model. In addition, we only considered four genes in our analysis. Higher-fold multiplex systems could be applied to consider a more complete signature of osteocyte response. While we used an objectively selected intensity threshold to classify osteocytes with high or low gene expression, our results may be sensitive to the threshold. As such, we tested the sensitivity of the results to this value. While raising or lowering this threshold decreased and increased, respectively, the magnitude of the differences in the mechanical stimuli surrounding the osteocytes, differences were still detected (Supplemental Fig. 7). Another limitation of the study is that registration was done

Gene response	Strain measure	R^2	*p*
SOST	Deviatoric	0.101	4.0×10^{-11}
	Hydrostatic	0.046	4.7×10^{-10}
	Hydrostatic gradient	0.125	3.3×10^{-13}
Wnt11	Deviatoric	0.056	1.2×10^{-15}
	Hydrostatic	0.672	2.0×10^{-16}
	Hydrostatic gradient	0.041	3.0×10^{-9}
SOST + Wnt11	Deviatoric	0.0822	2.0×10^{-16}
	Hydrostatic	0.0419	2.0×10^{-16}
	Hydrostatic gradient	0.0775	2.0×10^{-16}
TNF	Deviatoric	0.032	2.0×10^{-16}
	Hydrostatic	0.006	4.0×10^{-15}
	Hydrostatic gradient	0.013	2.6×10^{-12}
FRZB	Deviatoric	0.037	8.6×10^{-18}
	Hydrostatic	0.010	3.0×10^{-5}
	Hydrostatic gradient	0.021	7.5×10^{-11}
FRZB + TNF	Deviatoric	0.0356	2.0×10^{-16}
	Hydrostatic	0.00656	4.3×10^{-6}
	Hydrostatic gradient	0.00656	3.9×10^{-6}

Table 2. Logistic regression outcomes for differential expression of genes or combinations of gens from baseline versus each mechanical stimulus.

manually. However, we showed that the results are not sensitive to the size of the mesh (Supplemental Fig. 8), and therefore, small misalignments of the sections would not have a large effect the results.

We looked at three genes—SOST, Wnt11, and FRZB (secreted Frizzled Related Protein 3)—that affect Wnt signaling, which is central to osteoblast differentiation[44,51–54]. Transcriptionally, these three genes are regulated independently of one another, and could potentially be regulated by different magnitudes or modes of tissue deformation. SOST codes for the protein sclerostin which is an antagonist of the Wnt/B-catenin signaling pathway, a major driver of osteoblastogenesis[44,55]. FRZB is also a Wnt antagonist that binds to soluble Wnt proteins or to Frizzled on the cell membrane to modulate Wnt signaling[53,54]. However, FRZB can also enhance diffusion of Wnts[56] In contrast, Wnt11 acts on the non-canonical Wnt pathway to regulate R-spondin 2 which is necessary for canonical Wnt signaling and osteoblastogenesis[47,51]. We also measured TNF (Tumor Necrosis Factor) expression, which is primarily associated with osteoclastogenesis[57]. However, when TNF binds to its membrane receptor it can act on the SOST promotor through NFKB[57]. We did not measure protein expression of TNF, and cannot say whether this pathway played a role in SOST gene expression in this system.

While the response of individual genes is highly heterogeneous, we found that when two genes were differentially regulated from their baseline expression (*i.e.* Wnt11-high/SOST-low and FRZB-low/TNF-low) the associated tissue mechanical stimuli were higher than where a single gene responded, which were in turn higher than those surrounding osteocytes where neither gene changed from its baseline (*i.e.* Wnt11-low/SOST-high and FRZB-high/TNF-high). This suggests that some stochastic gene expression occurs, but when multiple differentially regulated genes are detected, that mechanical regulation is more likely to be the cause.

Deviatoric strain, hydrostatic strain, and the hydrostatic strain gradient were all moderately correlated with each other, making it difficult to isolate their effects. The logistic regressions indicated that all three strain measures were significant but weak predictors of gene expression. The weak regressions reflect that the mechanical measures were heterogeneous, that the baseline gene expression may vary, and that osteocytes may influence gene expression in their neighbors through gap junction communication. However, the hydrostatic strain gradient surrounding nearly all SOST High cells was very low (about 4.2 μ-strain/μm vs. 6.0 μ-strain/μm). This suggests that the hydrostatic strain gradient, and hence fluid flow, is associated with downregulation of SOST, while the other genes may respond to different strain measures or combinations of strain measures.

The relationship between strain gradient and gene expression supports Weinbaum's hypothesis that fluid flow through the lacunar-canalicular network is the physical stimulus sensed by osteocytes[42,58–60]. Theoretical and computational models indicate that the shear stress reaches magnitudes of 8–30 dyn/cm[258–60], which is similar to the shear stress experienced by other cells in which an intracellular Ca^{2+} response has been observed[61].

The differentially expressed genes detected in in vitro studies that employ fluid flow across the surface of osteocytes to study their response to loading[62–65] do not always reflect the in vivo or in situ studies[29,30,28]. This may be because both baseline gene expression and response to mechanical loads differ between 2-D and 3-D culture[66]. Our in situ culture system allowed us to pinpoint specific mechanical stimuli in a physiologically relevant loading scheme, while being able to control the loading more tightly than in an in vivo study.

Our data provide further insight into in vivo studies of bone formation in murine models with respect to local strain. Although bone formation was found in only 30 to 50% of regions with high strain energy density, formation was more common than quiescence or resorption in those regions[45,46]. Our data show that the osteocyte response is more strongly related to strain or strain gradient than this. We hypothesize that diffuse

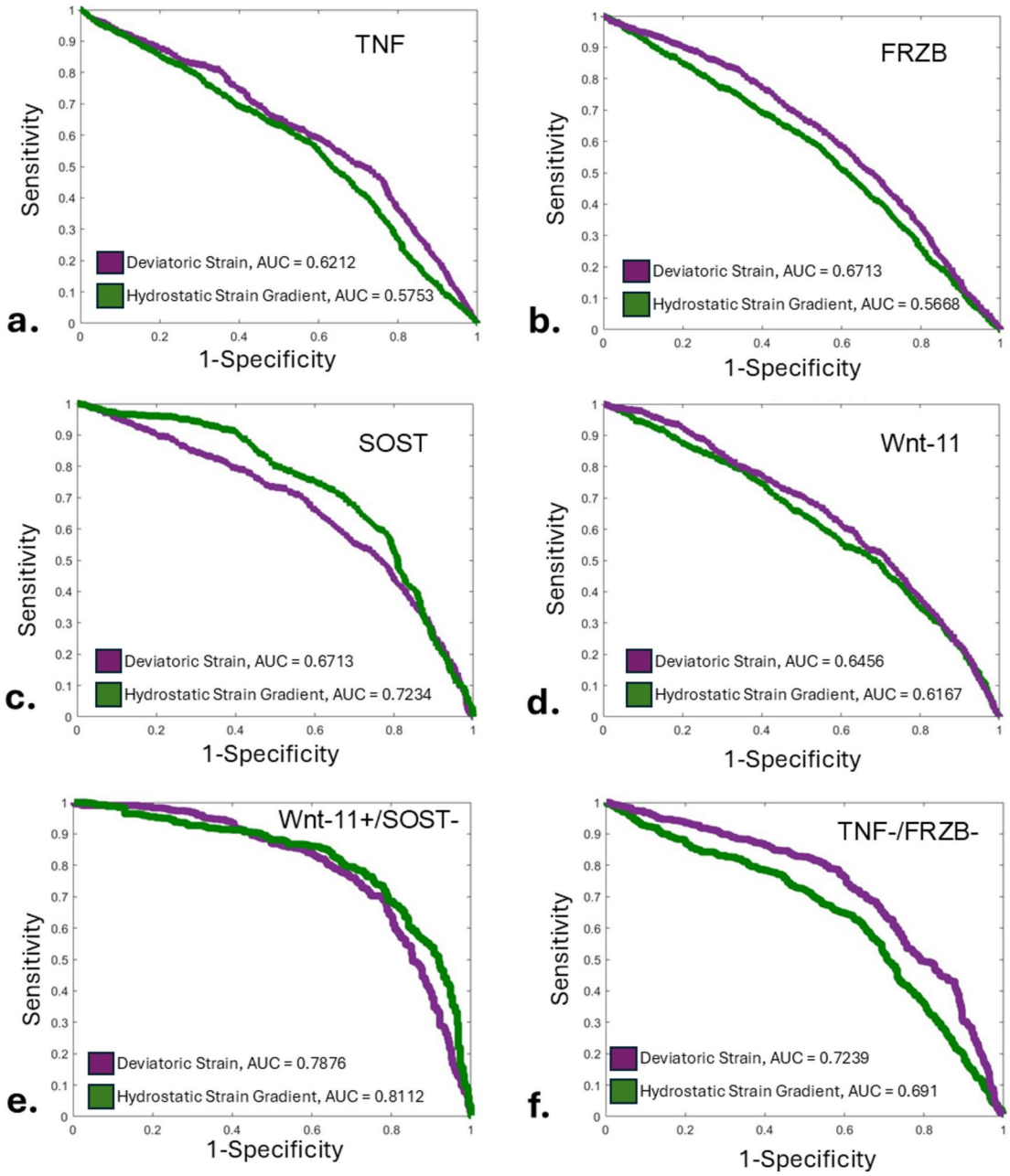

Fig. 6. ROCs indicate that deviatoric strain and hydrostatic strain gradient were both relatively weak discriminators of altered TNF (**a**) and FRZB (**b**) expression. Altered SOST expression was better identified by strain gradient (**c**), while Wnt11 expression was similarly discriminated by each measure (**d**). Excluding the osteocytes where only one gene was altered increased the AUC in all cases. (**e**) Hydrostatic strain gradient was a better predictor than deviatoric strain for combined SOST and Wnt11 expression than deviatoric strain. (**f**) Deviatoric strain was a better predictor of TNF + FRZB expression than hydrostatic strain gradient.

transport of the signaling molecules to progenitor cells, imprecise targeting of cell migration, or failure to control the lifetime of the bone multicellular units might explain some of the stochastic aspects of formation[67]. Our data also indicates some untargeted osteocyte response (i.e. large standard deviations), which may be due to intracellular communication among osteocytes or to normal variations in the baseline gene transcription.

Our results also complement a recent study that found that SOST expression was reduced in a mouse tibial loading model[68]. However, in contrast to our results, they found that SOST expression was higher in the mid-diaphysis of the tibia, where the bone was subjected to higher deformation and strain gradient than would occur near the metaphysis. They suggest that osteocytes may respond to loading differently depending on their previous loading history, which is plausible based on RNAseq data[29,30].

SOST gene expression exhibited an approximate on–off behavior in our study, with high expression corresponding to a relatively narrow range of strain gradient, and a very weak correlation with strain gradient.

Wnt11 gene expression was similarly poorly correlated to strain gradient but elevated at high strains. This is consistent with Ca^{2+} flux—an early secondary messenger response—in osteocytes in loaded mouse metatarsals, where the intensity of the response did not depend on load magnitude for strain levels in the range we studied here, but more cells responded as the peak strain increased[25]. Three-point bending induces a strain field that increases linearly both from the neutral bending axis to the upper and lower surfaces of the bone and from the outer supports to the center loading point. As such, their observation that the number of cells increased without spatial dependence on the strain could be further evidence of strain gradient rather than strain dependence.

When synthesized with previous studies, our data provide strong evidence that mechanotransduction in osteocytes is related to fluid flow in the lacunar-canilicular network. Fluid flow in porous solids depends strongly on strain gradients and strain rate (e.g. frequency in cyclic loading), and the concomitant dependence of gene expression and Ca^{2+} flux on these parameters, respectively, supports a fluid flow mediated mechanism. Further studies of osteocyte response in in situ or in vivo models where a functional lacunar-canalicular network is present are needed to further understand this mechanism.

Methods

Bone preparation and culture

Cervical spines from 8 female pigs around 9 mon of age were obtained from a local abattoir (Martin's Custom Butchering, Wakarusa, IN) within one hour of slaughter. Male pigs were excluded because male pigs are typically castrated at a young age and the effects of castration on bone physiology are unknown. Cylindrical trabecular bone explants, 8 mm in diameter, were excised from the C3, C4, and C5 vertebrae using a diamond coring bit under constant irrigation with cold saline supplemented with 3% antibiotic/antimycotic (10,000 units/mL of penicillin, 10,000 µg/mL of streptomycin, and 25 µg/mL of Amphotericin B, Corning Inc.). The cores were parallel to the axis of the vertebral body which is the primary loading axis of the bone in vivo and coincides with the principal trabecular orientation. Both ends of the explants were cut flat and parallel using a diamond wafering saw to a final length of 10 mm.

The prepared explants were cultured in a custom compression bioreactor[12]. Explants were bathed in high glucose (4.5 g/L) DMEM (Corning) with 10% FBS (Hyclone), and 1% AB/AM (Corning) circulating at a rate of 45 mL/hr.

Explants were equilibrated for 48 h with no load to allow the osteocytes to establish a baseline gene expression. Starting on day 3, four explants were subjected to cyclic compressive loading using an electromagnetic load frame (TA Instruments, Electroforce 5500, New Castle) with a 4 Hz rest inserted triangle wave pattern[48]. Explants were loaded twice a day, except on day 5 when they were loaded once, for 5 min using a 4 Hz rest inserted triangle wave from 10 to 200 N (0.20 to 3.98 MPa). The average load achieved by the controller was 195 ± 3N (3.87 ± 0.06 MPa). Four additional control explants were cultured without loading. Explants were fixed in 10% neutral buffered formalin for 48 h at 4 °C.

Finite element model

Micro-computed tomography images of the fixed implants were obtained at 20 µm resolution to capture the geometry for finite element analysis. The X-ray source was set at 70 kVp and 114 mA current and 200 ms integration time. Reconstructed mages were Gaussian filtered with a variance of 0.8 and support of 2.0, and segmented using a fixed threshold of 210/1000, which corresponds to a mineral density of 252 mg HA/cm^3 on our scanner. Finite element models were created from the micro-CT scans to quantify the strain in the bone tissue. Voxel-based meshes were created directly from the thresholded volume with 20 × 20 × 20 µm hexahedral elements. The mean trabecular thickness (Tb.Th*) of the loaded samples was 133 ± 17 µm, which was over six times the element size, indicating that the stress and strain fields were converged[69,70]. The bone was modeled as an isotropic linear elastic material, with the modulus of each element calculated based on the mineralization of the bone at that voxel[71]. The Poisson's ratio was set to 0.3. The explant specific displacement measured during loading was applied as a compressive boundary condition with free lateral expansion. The models were solved with our custom software[35,69] and the deviatoric and hydrostatic strain were subsampled within each element to obtain strains and strain gradients at 10 µm resolution, which is approximately the size of an osteocyte. The hydrostatic strain gradient was calculated using the Image Gradient Magnitude function in VTK (Kitware, Clifton Park, New York) as a surrogate measure of poroelastic fluid flow (Fig. 3). The relationship between strain gradient and fluid flow is based on linear poroelasticity theory (c.f.[72] where the fluid pressure, p, depends on the change in the fluid mass from the reference, ζ, the trace of the strain tensor $\boldsymbol{E}$, which is 3 times the hydrostatic strain, and Λ, a scalar combination of the bulk moduli of the solid and fluid components:

$$p = \frac{(\zeta - tr\boldsymbol{E})}{\Lambda} \tag{1}$$

The fluid flow rate, $\boldsymbol{q}$, depends on the pressure gradient according to Darcy's law:

$$\boldsymbol{q} = \boldsymbol{K}\nabla p = (\nabla\zeta - \nabla trE)/\Lambda \tag{2}$$

where $\boldsymbol{K}$, is a 2nd order tensor of permeability coefficients and ∇ is the spatial gradient operator. Note that ζ depends on fluid flow and changes with time until the gradient of fluid content change is equal to three times the gradient of the hydrostatic strain gradient. We assumed that the fluid flows primarily through the lacunar-canalicular pores although we did not directly model the flow, which would require a multiscale model[39,73,74].

Fluorescence in situ hybridization

Explants were demineralized in Ethylenediaminetetraacetic acid (EDTA) for approximately 3 weeks. EDTA was replaced weekly, and the mineralization was verified by X-ray. Explants were removed from the EDTA once micro-CT showed that the explants were fully demineralized. Explants were embedded in paraffin such that the sections were perpendicular to the axis of loading. The embedded explants were sectioned at a thickness of 5 μm and affixed to Vectabond treated SuperFrost slides and allowed to dry.

In situ hubridization was performed using the ACDBio RNAScope® Multiplex kit (Biotechne, Minneapolis, MN). Tissue sections were warmed in an oven at 60 °C to prior to rehydration in xylene (2 × 5 min), 100% ethanol (2 × 5 min), 90% ethanol (2 × 5 min), and 70% ethanol (2 × 5 min). A barrier was drawn around each section using a hydrophobic pen (ImmEdge, Vector Laboratories, Newark, CA). In lieu of the standard protease and antigen retrieval step, a custom treatment specifically formulated for bone by ACDBio was used. The slide was submerged in this solution for 30 min at 40 °C in a prewarmed humidity control tray (HybEZ oven, ACDBio) containing dampened filter paper.

Custom probes for porcine TNF, FRZB, SOST, and Wnt11 were designed and obtained from ACDBio (Supplemental Table 3). TNF and FRZB probes were applied to half the slides while SOST and Wnt11 probes were applied to the other half. Autofluorescence of the bone did not allow for visualization of more than two probes for each section. The slides were incubated at 40° C for two hours, then washed in RNAScope® wash buffer. Each channel was amplified using its respective reagent. Opal 520 and Cy3 fluorophores were conjugated to the two channels. Each section was then incubated in DAPI for 1 min prior to cover slipping using Cytoseal. The slides were stored at 4 °C protected from light until they were imaged.

The sections imaged on a Nikon AXR confocal microscope. Fifteen individual images of 0.61 mm^2 were taken of each section. The Opal 520 dye was imaged using the FITC filter, and the Cy3 dye was imaged using the TRITC filter. The sections were also imaged in the brightfield channel using phase contrast to identify the osteocyte cell body.

A negative control probe was used with both fluorophores to validate that there was minimal non-specific binding of the fluorophores in osteocytes, although some non-specific fluorescence was observed in the marrow (Supplemental Fig. 9).

Image processing and analysis

The z-stack for each channel was projected using the Maximum Intensity Projection function in ImageJ and saved as a separate image. Image masks were created by thresholding the phase contrast brightfield images to identify the lacuna locations. Two images from each section were manually analyzed to determine the efficacy of the workflow in ImageJ, demonstrating a 5.1% false positive rate and a 9.8% false negative rate. The mask was applied to the individual fluorescence channels using the Image Processing Toolbox in Matlab (Mathworks, Natick, MA), to label image pixels belonging to individual osteocytes. For each osteocyte, the average intensity of the pixels within the boundary of the osteocyte was calculated for each channel. The intensity level was used as a measure of the relative level of expression of that gene (Supplemental Fig. 1).

Probability density functions were fit to histograms of the intensity level of each gene in the pooled osteocytes from the loaded and unloaded bones using the fitdist() function and kernel density method in Matlab (Mathworks, Natick, MA). The kernel density method is a non-parametric method to estimate the probability density function of a variable. The intensity where the probability density functions of the loaded and unloaded explants intersected for each gene was used to classify osteocytes as having either high or low expression of that gene.

The RNAScope® images were manually registered to the corresponding location on the finite element model result images. The resolution of the registered confocal images was adjusted to the corresponding 10 μm resolution of the model results. For each pixel in the cross-section corresponding to an osteocyte, the strains and the strain gradient of the eight surrounding pixels were averaged to determine the strain associated with that osteocyte.

We modeled the binary of high expressing and low expressing osteocytes using logistic regression[75]. We also constructed receiver operator characteristic (ROC) curves and calculated the area under the curve (AUC-ROC) to determine whether the strain measures were predictive of gene expression level.

Data availability

The original data is available on the public archive: https://doi.org/https://doi.org/10.7274/28030580

Received: 30 December 2024; Accepted: 25 April 2025
Published online: 27 May 2025

References

1. Roux, W. *Die Entwicklungsmechanik; Ein Neuer Zweig Der Biologischen Wissenschaft* Vol. 1 (Wilhelm Engelmann, 1905).
2. Wolff, J. *Das Gesetz Der Transformation Der Knochen* (Hirschwald, 1892).
3. Wolff, J. *The law of bone remodelling* (Springer-Verlag, 1986).
4. Nowlan, N. C., Murphy, P. & Prendergast, P. J. Mechanobiology of embryonic limb development. *Ann. N. York Acad. Sci.* **1101**, 389–411 (2007).
5. Verbruggen, S. W. et al. Stresses and strains on the human fetal skeleton during development. *J. R. Soc. Interface* **15,** (2018).
6. Carter, D. R., Van Der Meulen, M. C. & Beaupre, G. S. Mechanical factors in bone growth and development. *Bone* **18**, 5S-10S (1996).
7. Meulen, M. C. V. D. Mechanics in skeletal development, adaptation and disease. Philosophical transactions of the Royal Society of London. *Ser. A Math. Phys. Eng. Sci.* **358**(1766), 565–578 (2000).

8. van der Meulen, M. C., Beaupre, G. S. & Carter, D. R. Mechanobiologic influences in long bone cross-sectional growth. *Bone* **14**, 635–642 (1993).
9. Martin, B. A theory of fatigue damage accumulation and repair in cortical bone. *J. Orthop. Res.* **10**, 818–825 (1992).
10. Martin, B. Mathematical model for repair of fatigue damage and stress fracture in osteonal bone. *J. Orthop. Res.* **13**, 309–316 (1995).
11. Anani, T. & Castillo, A. B. Mechanically-regulated bone repair. *Bone* **154**, 116223 (2022).
12. Claes, L. E. et al. Effects of mechanical factors on the fracture healing process. *Clin. Orthop. Relat. Res.* **355S**, S132–S147. https://doi.org/10.1097/00003086-199810001-00015 (1998).
13. Morgan, E. F., Gleason, R. E., Hayward, L. N. M., Leong, P. L. & Palomares, K. T. S. Mechanotransduction and fracture repair. *J. Bone Jt. Surg.* **90**, 25–30 (2008).
14. Liu, X. & Niebur, G. L. Bone ingrowth into a porous coated implant predicted by a mechano-regulatory tissue differentiation algorithm. *Biomech. Model. Mechanobiol.* **7**, 335–344 (2008).
15. Mukherjee, K. & Gupta, S. Influence of implant surface texture design on peri-acetabular bone ingrowth: A mechanobiology based finite element analysis. *J. Biomech. Eng.* **139**, 031006 (2017).
16. Lynch, M. & Fischbach, C. Biomechanical forces in the skeleton and their relevance to bone metastasis: Biology and engineering considerations. *Adv. Drug Deliv. Rev.* **79–80**, 119–134 (2014).
17. Lynch, M. E. et al. In vivo tibial compression decreases osteolysis and tumor formation in a human metastatic breast cancer model. *J. Bone Miner. Res.* **28**, 2357–2367 (2013).
18. Coughlin, T. R. et al. Bone: A fertile soil for cancer metastasis. *Curr. Drug Targets* **18**, 1281–1295 (2017).
19. Schaffler, M. B. & Kennedy, O. D. Osteocyte signaling in bone. *Curr. Osteoporos. Rep.* **10**, 118–125 (2012).
20. Kennedy, O. D. & Schaffler, M. B. The roles of osteocyte signaling in bone. *J Am. Acad. Orthop. Surg.* **20**, 670–671 (2012).
21. Bonewald, L. F. The amazing osteocyte. *J. Bone Miner. Res.* **26**, 229–238 (2011).
22. Curtis, K. J., Oberman, A. G. & Niebur, G. L. Effects of mechanobiological signaling in bone marrow on skeletal health. *Ann. N. Y. Acad. Sci.* **1460**, 11–24 (2020).
23. Curtis, K. J., Coughlin, T. R., Varsanik, M. A. & Niebur, G. L. Shear stress in bone marrow has a dose dependent effect on cFos gene expression in in situ culture. *Cell. Mol. Bioeng.* **12**, 559–568 (2019).
24. Curtis, K. J., Coughlin, T. R., Mason, D. E., Boerckel, J. D. & Niebur, G. L. Bone marrow mechanotransduction in porcine explants alters kinase activation and enhances trabecular bone formation in the absence of osteocyte signaling. *Bone* **107**, 78–87 (2018).
25. Lewis, K. J. et al. Osteocyte calcium signals encode strain magnitude and loading frequency in vivo. *Proc. Natl. Acad. Sci. U.S.A.* **114**, 11775–11780 (2017).
26. Sato, T. et al. A FAK/HDAC5 signaling axis controls osteocyte mechanotransduction. *Nat. Commun.* **11**, 3282 (2020).
27. Gould, N. R. et al. Disparate bone anabolic cues activate bone formation by regulating the rapid lysosomal degradation of sclerostin protein. *Elife* https://doi.org/10.7554/eLife.64393 (2021).
28. Zhang, C. et al. Mapping the response of human osteocytes in native matrix to mechanical loading using RNA sequencing. *J. Bone Mineral Res. Plus* **7**(4), e10721. https://doi.org/10.1002/jbm4.10721 (2023).
29. Machireddy, M. et al. Controlled mechanical loading affects the osteocyte transcriptome in porcine trabecular bone in situ. *Bone* **181**, 117028 (2024).
30. Chermside-Scabbo, C. J. et al. Old mice have less transcriptional activation but similar periosteal cell proliferation compared to young-adult mice in response to in vivo mechanical loading. *J. Bone Miner. Res.* **35**, 1751–1764 (2020).
31. Milgrom, C. et al. The effect of muscle fatigue on in vivo tibial strains. *J. Biomech.* **40**, 845–850 (2007).
32. Burr, D. B. et al. In vivo measurement of human tibial strains during vigorous activity. *Bone* **18**, 405–410 (1996).
33. Morgan, E. F., Yeh, O. C. & Keaveny, T. M. Damage in trabecular bone at small strains. *Eur. J. Morphol.* **42**, 13–21 (2005).
34. Baumann, A. P., Shi, X., Roeder, R. K. & Niebur, G. L. The sensitivity of nonlinear computational models of trabecular bone to tissue level constitutive model. *Comput. Methods Biomech. Biomed. Engin.* **19**, 465–473 (2016).
35. Niebur, G. L., Feldstein, M. J., Yuen, J. C., Chen, T. J. & Keaveny, T. M. High resolution finite element models with tissue strength asymmetry accurately predict failure of trabecular bone. *J. Biomech.* **33**, 1575–1583 (2000).
36. Bacabac, R. G. et al. Round versus flat: bone cell morphology, elasticity, and mechanosensing. *J. Biomech.* **41**, 1590–1598 (2008).
37. Xie, J. et al. Compliant substratum changes osteocyte functions: The role of ITGB3/FAK/β-catenin signaling matters. *ACS Appl. Bio. Mater.* **1**, 792–801 (2018).
38. Zhang, D. et al. Extracellular matrix elasticity regulates osteocyte gap junction elongation: Involvement of paxillin in intracellular signal transduction. *Cell. Physiol. Biochem.* **51**, 1013–1026 (2018).
39. Verbruggen, S. W., Garrigle, M. J. M., Haugh, M. G., Voisin, M. C. & McNamara, L. M. Altered mechanical environment of bone cells in an animal model of short- and long-term osteoporosis. *Biophys. J.* **108**, 1587–1598 (2015).
40. McNamara, L. M., Majeska, R. J., Weinbaum, S., Friedrich, V. & Schaffler, M. B. Attachment of osteocyte cell processes to the bone matrix. *Anat. Record Adv. Integr. Anat. Evol. Biol.* **292**(3), 355–363 (2009).
41. Wang, Y., McNamara, L. M., Schaffler, M. B. & Weinbaum, S. A model for the role of integrins in flow induced mechanotransduction in osteocytes. *Proc. Natl. Acad. Sci. U.S.A.* **104**, 15941–15946 (2007).
42. Weinbaum, S., Cowin, S. C. & Zeng, Y. A model for the excitation of osteocytes by mechanical loading-induced bone fluid shear stresses. *J. Biomech.* **27**, 339–360 (1994).
43. Tate, M. L. Whither flows the fluid in bone? An osteocyte's perspective. *J. Biomech.* **36**, 1409–1424 (2003).
44. Robling, A. G., Bellido, T. & Turner, C. H. Mechanical stimulation in vivo reduces osteocyte expression of sclerostin. *J. Musculoskelet. Neuronal Interact.* **6**, 354 (2006).
45. Cresswell, E. N., Goff, M. G., Nguyen, T. M., Lee, W. X. & Hernandez, C. J. Spatial relationships between bone formation and mechanical stress within cancellous bone. *J. Biomech.* **49**, 222–228 (2016).
46. Schulte, F. A. et al. Local mechanical stimuli regulate bone formation and resorption in mice at the tissue level. *PLoS ONE* **8**, e62172 (2013).
47. Webster, D., Schulte, F. A., Lambers, F. M., Kuhn, G. & Müller, R. Strain energy density gradients in bone marrow predict osteoblast and osteoclast activity: a finite element study. *J. Biomech.* **48**, 866–874 (2015).
48. Yang, H., Embry, R. E. & Main, R. P. Effects of loading duration and short rest insertion on cancellous and cortical bone adaptation in the mouse tibia. *PLoS ONE* **12**, e0169519 (2017).
49. Cardoso, L., Fritton, S. P., Gailani, G., Benalla, M. & Cowin, S. C. Advances in assessment of bone porosity, permeability and interstitial fluid flow. *J. Biomech.* **46**, 253–265 (2013).
50. Tate, M. L. K., Steck, R., Forwood, M. R. & Niederer, P. In vivo demonstration of load-induced fluid flow in the rat tibia and its potential implications for processes associated with functional adaptation. *J. Exp. Biol.* **203**, 2737–2745 (2000).
51. da Silva, C. C. et al. Wnt11, a new gene associated with early onset osteoporosis, is required for osteoblastogenesis. *Hum. Mol. Genet.* **31**, 1622–1634 (2022).
52. Rui, S. et al. Phosphate promotes osteogenic differentiation through non-canonical Wnt signaling pathway in human mesenchymal stem cells. *Bone* **164**, 116525. https://doi.org/10.1016/j.bone.2022.116525 (2022).
53. Lories, R. J. U. et al. Articular cartilage and biomechanical properties of the long bones in Frzb-knockout mice. *Arthritis Rheum.* **56**, 4095–4103 (2007).
54. Thysen, S., Cailotto, F. & Lories, R. Osteogenesis induced by frizzled-related protein (FRZB) is linked to the netrin-like domain. *Lab. Investig.* **96**, 570–580 (2016).

55. Sebastian, A. & Loots, G. G. Transcriptional control of SOST in bone. *Bone* **96**, 76–84 (2017).
56. Mii, Y. & Taira, M. Secreted frizzled-related proteins enhance the diffusion of Wnt ligands and expand their signalling range. *Development* **136**(24), 4083–4088. https://doi.org/10.1242/dev.032524 (2009).
57. Zhao, B. TNF and bone remodeling. *Curr. Osteoporos. Rep.* **15**, 126–134 (2017).
58. Cowin, S. C., Weinbaum, S. & Zeng, Y. A case for bone canaliculi as the anatomical site of strain generated potentials. *J. Biomech.* **28**, 1281–1297 (1995).
59. Wang, L., Cowin, S. C., Weinbaum, S. & Fritton, S. P. Modeling tracer transport in an osteon under cyclic loading. *Ann. Biomed. Eng.* **28**, 1200–1209 (2000).
60. Zeng, Y., Cowin, S. C. & Weinbaum, S. A fiber matrix model for fluid flow and streaming potentials in the canaliculi of an osteon. *Ann. Biomed. Eng.* **22**, 280–292 (1994).
61. Anderson, E. J., Kaliyamoorthy, S., Iwan, J., Alexander, D. & Tate, M. L. K. Nano–microscale models of periosteocytic flow show differences in stresses imparted to cell body and processes. *Ann. Biomed. Eng.* **33**, 52–62 (2005).
62. Govey, P. M., Kawasawa, Y. I. & Donahue, H. J. Mapping the osteocytic cell response to fluid flow using RNA-Seq. *J. Biomech.* **48**, 4327–4332 (2015).
63. Govey, P. M. et al. Integrative transcriptomic and proteomic analysis of osteocytic cells exposed to fluid flow reveals novel mechano-sensitive signaling pathways. *J. Biomech.* **47**, 1838–1845 (2014).
64. Kamel, M. A., Picconi, J. L., Lara-Castillo, N. & Johnson, M. L. Activation of β-catenin signaling in MLO-Y4 osteocytic cells versus 2T3 osteoblastic cells by fluid flow shear stress and PGE2: Implications for the study of mechanosensation in bone. *Bone* **47**, 872–881 (2010).
65. Yan, Z. et al. Fluid shear stress improves morphology, cytoskeleton architecture, viability, and regulates cytokine expression in a time-dependent manner in MLO-Y4 cells. *Cell Biol. Int.* **42**, 1410–1422 (2018).
66. Zhang, C., Bakker, A. D., Klein-Nulend, J. & Bravenboer, N. Studies on osteocytes in their 3D native matrix versus 2D in vitro models. *Curr. Osteoporos. Rep.* **17**, 207–216 (2019).
67. Sims, N. A. & Vrahnas, C. Regulation of cortical and trabecular bone mass by communication between osteoblasts, osteocytes and osteoclasts. *Arch. Biochem. Biophys.* **561**, 22–28 (2014).
68. Chlebek, C., Moore, J. A., Ross, F. P. & van der Meulen, M. C. H. Molecular identification of spatially distinct anabolic responses to mechanical loading in murine cortical bone. *J. Bone Miner. Res.* **37**, 2277–2287 (2022).
69. Niebur, G. L., Yuen, J. C., Hsia, A. C. & Keaveny, T. M. Convergence behavior of high-resolution finite element models of trabecular bone. *J. Biomech. Eng.* **121**, 629–635 (1999).
70. Guldberg, R. E., Hollister, S. J. & Charras, G. T. The accuracy of digital image-based finite element models. *J. Biomech. Eng.* **120**, 289–295 (1998).
71. Hernandez, C. J., Beaupré, G. S., Keller, T. S. & Carter, D. R. The influence of bone volume fraction and ash fraction on bone strength and modulus. *Bone* **29**, 74–78 (2001).
72. Cowin, S. C. & Doty, S. B. *Tissue Mechanics* (Springer, 2007).
73. Wu, X. et al. Mathematically modeling fluid flow and fluid shear stress in the canaliculi of a loaded osteon. *Biomed. Eng. OnLine* **15**, 149 (2016).
74. Smit, T. H. Finite element models of osteocytes and their load-induced activation. *Curr. Osteoporos. Rep.* **20**, 127–140 (2022).
75. Trott, S. (2020). Binary classification in R. Retrieved from https://seantrott.github.io/binary_classification_R/

Acknowledgements

This research was supported by the U.S. National Institute of Arthritis Musculoskeletal and Skin diseases (NIAMS) AR075937, U.S. National Cancer Institute (NCI) CA252878, and U.S. National Institute of General Medicine (NGM): GM143055

SN was supported by the Harper Cancer Research Institute Interdisciplinary Interface Training Program. We thank the Notre Dame Integrated Imaging Facility for microscopy resources.

Author contributions

MM performed the main experiments and drafted the manuscript, SN assisted with experimental methods and data presentation, LD and JLewis performed computational simulations and analyzed data, SC assisted with imaging, JLu supervised and performed statistical analyses, GLN conceived and supervised the project, and edited the manuscript. All authors reviewed the final manuscript.

Competing interests

The authors have no competing interests.

Additional information

Supplementary Information The online version contains supplementary material available at https://doi.org/10.1038/s41598-025-00214-z.

Correspondence and requests for materials should be addressed to G.L.N.